scientific reports

Check for updates

OPEN

A mixed-field formulation for modeling dielectric ring resonators and its application in optical frequency comb generation

Ergun Simsek✉, Alioune Niang, Raonaqul Islam, Logan Courtright, Pradyoth Shandilya, Gary M. Carter & Curtis R. Menyuk

We present a novel finite-difference frequency-domain formulation for accurate and efficient modal analysis of dielectric ring resonators, a critical component in microresonator-based optical frequency comb (OFC) generation. Unlike previous methods, our approach solves for both electric and magnetic fields simultaneously in cylindrical coordinates, eliminating spurious modes and ensuring high fidelity at material boundaries. The solver enables rapid computation of resonant modes without requiring manual input for azimuthal mode numbers, significantly streamlining dispersion engineering for OFC design. We validate our method against experimental data and the results generated with commercial solvers, demonstrating excellent agreement in effective indices, integrated dispersion, and resonance linewidths for silicon nitride resonators excited with lasers operating at 1060 nm and 1550 nm. Our results highlight the solver's utility in predicting anomalous dispersion and coupling dynamics, offering a robust tool for designing high-performance OFC devices.

Optical frequency combs (OFCs) are powerful tools that provide a set of discrete, equally spaced spectral lines, with the potential to revolutionize various fields such as precision spectroscopy[1–4], optical metrology[2,5,6], telecommunications[2], and quantum information processing[3,7]. The ability to generate and control OFCs with high stability and broad bandwidth has enabled the realization of optical clocks[5], frequency synthesis[1], and high-capacity data transmission systems[2]. Among various platforms for OFC generation, microresonator-based frequency combs–also known as Kerr combs, as illustrated in Fig. 1–have attracted significant attention due to their compact size, high Q-factors, and compatibility with photonic integration[2,6,8–10].

Designing resonator geometries that support broadband and low-noise frequency combs requires precise dispersion engineering, which in turn depends on accurate and efficient numerical simulation tools. Several numerical methods are available to model electromagnetic wave propagation in dielectric resonators, including time-domain techniques such as the finite-difference time-domain (FDTD) method[11,12], and frequency-domain methods such as the finite element method (FEM)[13–16], mode matching[17], and the finite-difference frequency-domain (FDFD) method[18–24]. Among these, FDTD is a general-purpose solver capable of modeling complex time-domain phenomena, including nonlinear frequency comb dynamics. However, for large-scale or high-Q resonators, its computational cost becomes prohibitive due to the need for fine spatial and temporal resolution over long simulation windows. This is why the most common method for analyzing optical frequency comb generation is typically handled in two steps. First, modal analysis is performed using numerical solvers such as the finite element method (FEM) or finite differences frequency domain (FDFD) method. These solvers are used to compute the electromagnetic field profiles and the corresponding effective refractive indices of the confined or resonant modes in both the bus waveguide[25] and the dielectric resonator. High accuracy in this step is crucial, as even slight errors in field profiles or indices can result in significant deviations in predicted resonant behavior and coupling dynamics. Second, the interaction between the waveguide and the resonator is analyzed using coupled mode theory (CMT), which enables an approximate yet powerful framework for evaluating coupling efficiency between the structures[9,26,27]. From the computed effective indices, we can derive important dispersion-related quantities such as the group index and integrated dispersion, which are essential for understanding the phase-matching conditions and the bandwidth over which efficient comb generation can occur[6,8,9]. Once the linear modal and coupling characteristics are understood, non-linear dynamics, particularly those that govern soliton formation and frequency comb evolution, are modeled by solving the Lugiato-Lefever equation (LLE)[10,28–32].

Department of Computer Science and Electrical Engineering, University of Maryland Baltimore County, Baltimore, MD 21250, USA. ✉email: simsek@umbc.edu

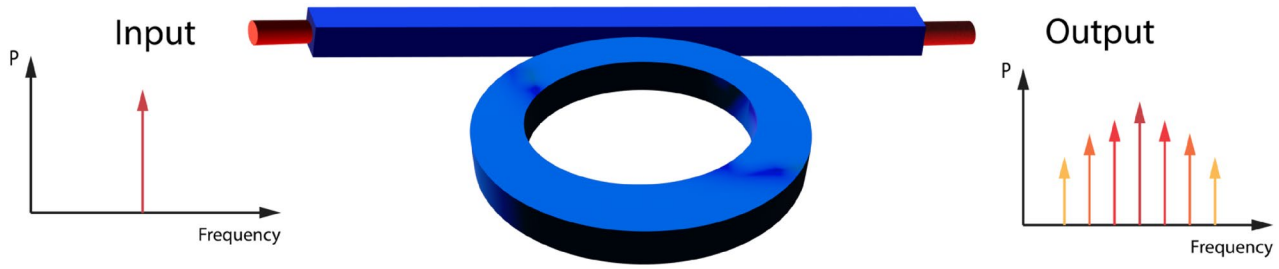

Fig. 1. Schematic illustration of optical frequency comb generation via bus waveguide coupled to a dielectric ring resonator. A continuous-wave (single-frequency) laser is launched into a bus waveguide (left), which is side-coupled to a dielectric ring resonator. Nonlinear interactions within the resonator lead to the generation of equidistant spectral lines, forming a frequency comb.

This equation incorporates both Kerr nonlinearity and dispersion, and its solution provides insight into the steady-state and transient behaviors of the system under realistic operating conditions.

Frequency-domain methods offer an attractive alternative for the linear modal analysis stage of design. Among the frequency-domain methods, FEM provides geometric flexibility for modeling irregular or curved waveguide cross-sections, though it requires sophisticated meshing and high-order basis functions. Mode matching divides the waveguide into subregions with known analytical modal solutions and enforces continuity at interfaces. While this approach avoids numerical dispersion errors, it often requires a large number of modes to converge in high-index-contrast structures. The FDFD method offers a favorable tradeoff between simplicity and accuracy. It uses structured grids to discretize Maxwell's equations directly, making it especially well-suited for exploratory design and research applications. Existing FDFD methods for axially symmetric structures typically operate either in cylindrical coordinates[19] or transformed Cartesian grids[18,20–24,33]. They usually solve for two transverse components of either the electric field (E)[19,22] or magnetic field (H)[21,23,24], with the remaining components inferred numerically. However, because resonant modes in dielectric rings are hybrid–lacking pure transverse-electric (TE) or transverse-magnetic (TM) character–field-only formulations may produce spurious modes. Solving for both E and H concurrently improves reliability by avoiding these artifacts.

In this work, we present a new formulation for electromagnetic wave propagation in dielectric rings and implement it in MATLAB using a finite-differences approach. Our solver enables rapid and accurate modal analysis in ring geometries, making it well-suited for exploring the dispersion characteristics essential for designing structures for optical frequency comb generation. As a first application, we investigated a dielectric ring resonator exhibiting anomalous dispersion near 1060 nm and successfully verified our numerical results against experimental data reported in a recent publication[6]. Subsequently, we applied our solver to study frequency comb generation near 1550 nm. The numerically obtained free spectral range (FSR) and full-width at half-maximum (FWHM) values show strong agreement with our experimental measurements, confirming the accuracy and utility of our method for frequency comb-related applications.

The importance of this work can be summarized as follows.

- Unlike some previous studies[19], our formulation accounts for the non-zero divergence of the electric field at material boundaries, ensuring more accurate field solutions.
- Unlike some earlier work[21,23,24], we derive the formulation in cylindrical coordinates; hence, we do not use the coordinate transformation approximation.
- Unlike it is done in earlier studies[33], our method does not neglect the field components in the direction of propagation, enabling a complete description of hybrid modes in dielectric resonators.
- Our solver concurrently computes the E and H fields, eliminating spurious modes and improving reliability.
- We rigorously benchmarked our numerical results against experimental data and the ones obtained with commercial solvers, COMSOL Multiphysics and Tidy3D.

Results

Figure 2 illustrates a dielectric ring with a central radius of R_c, width of w_r, and height of h_r. The background does not have to be a homogeneous medium. The ring can be placed on a substrate, for example, as illustrated in Fig. 2. The only requirement regarding the background is that it has to have cylindrical symmetry with respect to the z-axis. So, the relative permittivity (ε) is a function of ρ and z. We assume the entire structure is non-magnetic, i.e., $\mu(\rho, z) = \mu_0$, where μ_0 is the magnetic permeability of free space.

We discretize the computational domain along a rectangular grid by selecting N_ρ uniformly distributed samples along the ρ-direction and N_z uniformly distributed samples along the z-direction as shown in Fig. 2b. We compute the first- and second-order derivatives using central finite differences[25]. We place a perfectly matched layer around the boundary following the recipe developed by Berenger[34]. As explained on page 36 of Kogelnik's pioneering work[35], the fields outside the dielectric waveguides decay exponentially for the guided modes. Hence, placing the ring at the center of a computational domain that is $(w_r + \lambda) \times (h_r + \lambda)$, where w_r and h_r are the ring width and height, is sufficient to obtain accurate results to determine the resonant modes of a ring surrounded by a homogeneous background. However, if a thin film and/or substrate are present, the computational domain should be enlarged to adequately capture their effect on wave propagation.

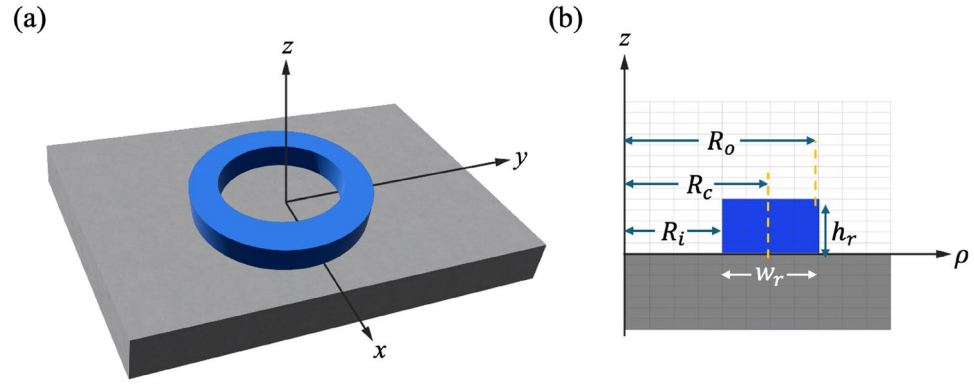

Fig. 2. A dielectric ring with a width of w_r, a height of h_r, and a central radius of R_c on a substrate: (**a**) three-dimensional and (**b**) two-dimensional views. R_i and R_o are the inner and outer radii of the ring, i.e., $R_i = R_c - w_r/2 = R_o - w_r$. By assuming the material properties are uniform axially around the z-axis, the problem can be solved in two dimensions using differential vector operators in the cylindrical coordinate system.

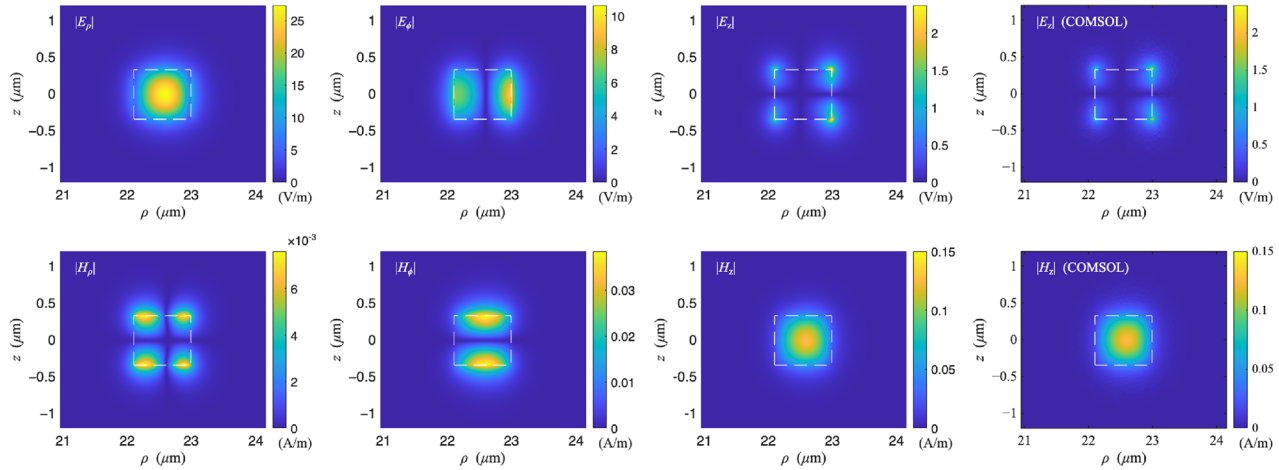

Fig. 3. Left three columns: magnitude of the electric (top row) and magnetic (bottom row) fields' ρ, ϕ, and z components for the first resonant mode of the electromagnetic waves computed with our solver. The last column shows $|E_z|$ and $|H_z|$ distributions obtained with COMSOL. The white dashed lines outline the boundaries of the ring, giving insight into how the electromagnetic fields are confined but not completely symmetric.

Integrated dispersion study

For the first example, we carry out modal analysis on the dielectric ring studied in a recent study[6]. The ring's outer radius, width, and height are 23 μm, 890 nm, and 670 nm, respectively. The ring is made from silicon nitride[4] (Si_3N_4) and surrounded by silicon dioxide[36] (SiO_2). For the numerical solution, we use a 430×320 grid which covers $5w_r$ by $5h_r$ region on the $\rho - z$ plane with a 100-point-per-wavelength (ppw) sampling density.

The first three columns of Fig. 3 show the magnitude of the electric (first row) and magnetic (second row) fields' ρ, ϕ, and z components on the $\rho - z$ plane for the first resonant mode obtained with our solver. In the last column, we provide field profile examples ($|E_z|$ and $|H_z|$) obtained with COMSOL. These solutions demonstrate a close agreement, with only minor deviations within acceptable numerical tolerance levels. We observe that the electric field is well-confined within the high-index Si_3N_4 region, with some fields extending slightly outside the boundaries due to the evanescent field. The symmetry of the fields is consistent with the fundamental resonant mode, where fields are strongly coupled to the geometry of the ring.

The results presented in Table 1 demonstrate a very good agreement between our solver and two widely used commercial solvers–COMSOL Multiphysics and Tidy3D–for the effective refractive indices of the first eight resonant modes. For both commercial solvers, a sampling density of 100 ppw is used. The computation domain (without the perfectly matched layers) is $5w_r$ by $5h_r$. For all modes, the effective index computed by our method closely matches those obtained from COMSOL and Tidy3D, with discrepancies typically on the order of 10^{-3} or less.

mode index	n_{eff} (COMSOL)	n_{eff} (Tidy3D)	n_{eff} (This work)
1	1.86881	1.86963	1.86854
2	1.85677	1.85748	1.85649
3	1.68341	1.68470	1.68332
4	1.66419	1.66551	1.66396
5	1.60776	1.60806	1.60755
6	1.55427	1.55503	1.55422
7	1.52296	1.52364	1.52292
8	1.49083	1.49179	1.49068

Table 1. Effective refractive indices of the first four resonant modes of a Si_3N_4 ring buried in SiO_2, computed with COMSOL, Tidy3D, and our solver.

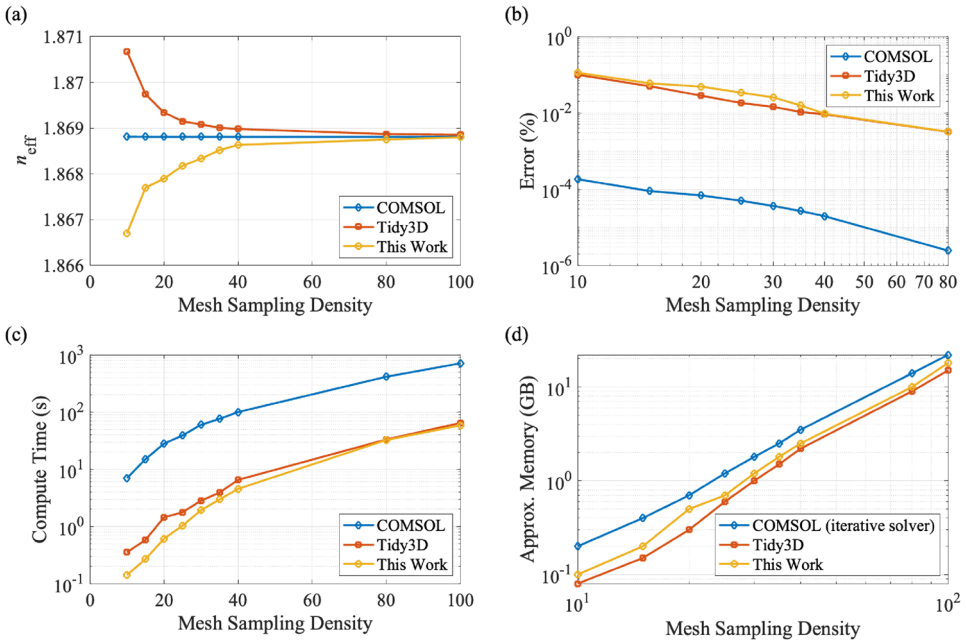

Fig. 4. Effective index of the first fundamental mode, relative error, compute time, and approximate memory usage of COMSOL Multiphysics (blue), Tidy3D (red), and our solver (yellow) as a function of mesh sampling density.

Figure 4 presents a comprehensive comparison of three electromagnetic solvers–COMSOL, Tidy3D, and the finite-difference frequency-domain (FDFD) solver developed in this work–evaluated in terms of effective index convergence (for the first fundamental mode), relative error, compute time, and approximate memory usage, all as functions of mesh sampling density, expressed in ppw.

In Fig. 4a, the convergence of the effective index is shown as a function of mesh density. COMSOL exhibits a stable and nearly flat convergence profile, approaching a value of 1.86881. Tidy3D shows monotonic convergence from above, while our FDFD solver converges from below. Around 100 points per wavelength (ppw), all three solvers converge to the same effective index, establishing consistency and validating the accuracy of the numerical approaches. Figure 4b presents the relative error in the effective index, plotted on a logarithmic scale. The reference solution is the COMSOL result obtained with the highest mesh density of 100 ppw, which is taken as the ground truth. COMSOL achieves the lowest relative error, dropping below 10^{-6}% as the mesh is refined. Tidy3D and our FDFD solver exhibit higher initial error levels, ranging from approximately 0.1% to 0.01%, but both show consistent improvement with mesh refinement. While Tidy3D performs slightly better at intermediate densities, our FDFD solver matches or surpasses its accuracy at higher mesh densities, achieving an error of less than 0.01% near 60 ppw. The observed slopes of the error curves indicate second-order convergence, consistent with the use of quadratic basis functions. Figure 4c compares the computation time per mode. COMSOL shows a steep increase in computation time with mesh refinement, exceeding several hundred seconds at the highest densities. In contrast, both Tidy3D and our FDFD solver are significantly faster, remaining below 100 seconds across all mesh densities. Two primary factors explain this differece: (i) the FEM solves for a single mode at a time, whereas FDFD solvers can compute multiple resonant modes simultaneously, and (ii) FEM relies on an unstructured mesh, which requires more time to assemble the system matrices compared to

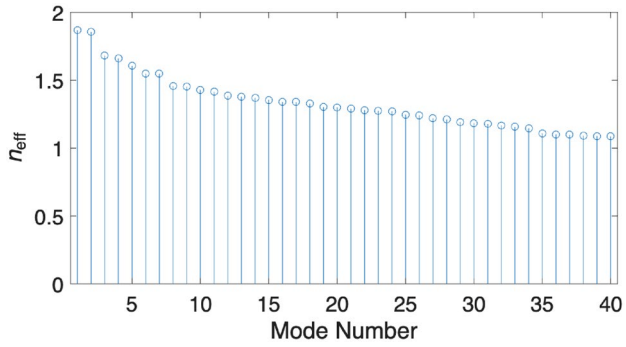

Fig. 5. The effective index of the first 40 modes computed with our solver.

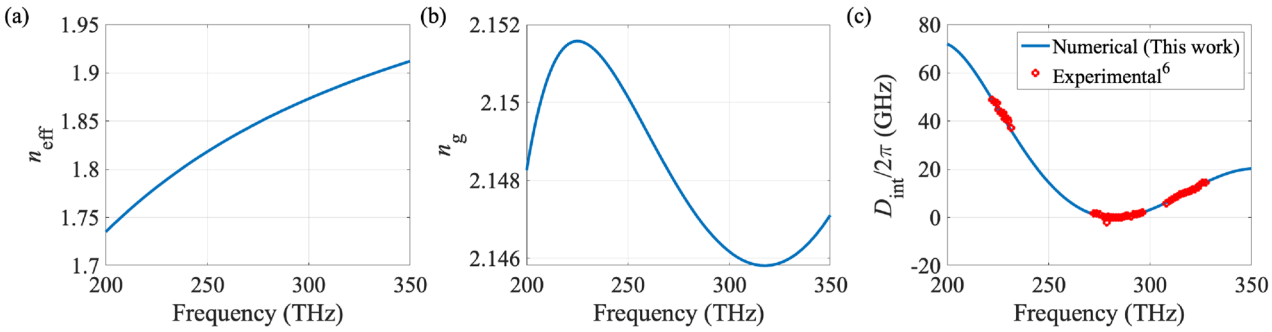

Fig. 6. (**a**) Effective refractive index n_{eff} as a function of frequency, computed using our numerical formulation. (**b**) Corresponding group index n_{g} derived from the wavelength dependence of n_{eff}. (**c**) Integrated dispersion $D_{\mathrm{int}}/2\pi$ in GHz compared with experimental measurements[6]. The pump frequency is 283 THz (1060 nm).

the uniform grid used in FDFD solvers. The latter enables faster matrix assembly and simpler memory access patterns. Our FDFD solver performs on par with, and occasionally better than, Tidy3D in the low to mid-range of mesh densities, demonstrating its efficiency and suitability for fast simulations. Approximate memory usage is plotted in Fig. 4d as a function of mesh density. All solvers exhibit near power-law scaling. COMSOL, despite employing an iterative solver, consumes the most memory, followed by our FDFD solver, which uses slightly more memory than Tidy3D. This is likely due to the simultaneous solution of both electric and magnetic field components in our implementation. FEM's high memory consumption stems from several factors: it requires storing and operating on sparse matrices corresponding to unstructured meshes, and these matrices tend to have a higher number of non-zero entries per row due to the use of high-order basis functions and irregular element connectivity. Additionally, the FEM formulation may involve more complex data structures to manage element connectivity, boundary conditions, and shape functions, which further contribute to increased memory demands.

To emphasize the main benefit of FDFD solvers compared to the FDTD solvers, let us provide another figure as follows. In conventional electromagnetic solvers such as ANSYS Lumerical and COMSOL Multiphysics, modal analysis of dielectric ring resonators requires an initial guess for the effective index (in ANSYS Lumerical) or azimuthal mode number (in COMSOL Multiphysics), which is approximately given by βR_c, where β is the unknown propagation constant. After finding one mode, users iteratively try neighboring integers to locate additional resonant modes. This trial-and-error process can be cumbersome and time-consuming. In contrast, our mathematical formulation eliminates the need for such manual input. By specifying only the number of desired modes, our solver automatically computes the corresponding field distributions and effective indices. As illustrated in Fig. 5, we efficiently obtained the effective indices of the first 40 modes in just four minutes on a standard 2021 Apple MacBook Pro with 32 GB of RAM, averaging 6 seconds per mode. This performance is comparable to COMSOL's computation time using a high-quality mesh of 30 points per wavelength, but without the burden of manual parameter tuning, providing a more streamlined and scalable approach to dielectric ring resonator analysis.

To characterize the dispersive properties of the dielectric ring resonator, we first compute the frequency-dependent effective refractive index, n_{eff}, using the proposed numerical formulation. The calculations are performed at 100 evenly spaced frequency points ranging from 200 THz to 350 THz. The resulting effective index profile is shown in Fig. 6a. From the effective index data, we derive the group index using the relation $n_{\mathrm{g}} = n_{\mathrm{eff}} - \lambda\, dn_{\mathrm{eff}}/d\lambda$, where λ is the corresponding wavelength. The computed group index is presented in Fig. 6b. Next, we calculate the integrated dispersion, defined as the deviation of the resonant frequencies

from a perfectly equidistant grid: $D_{\text{int}}(\mu) = \omega_\mu - (\omega_0 + D_1\mu)$, where ω_μ denotes the angular frequency of the μ^{th} resonant mode, ω_0 is the pump frequency (set to 283 THz, corresponding to 1060 nm), and D_1 is the free spectral range (FSR) at the pump frequency in rad/s. By fitting the calculated values of $D_{\text{int}}(\mu)$ to a polynomial expansion, we extract the second-order dispersion parameter D_2, whose positive sign indicates the anomalous dispersion regime–a necessary condition for soliton formation in microresonator-based optical frequency combs. The computed integrated dispersion is shown in Fig. 6c. Our numerical results (blue curve) exhibit a good agreement with the experimental data[6], which are overlaid as red circular markers.

Figure 7 shows the integrated dispersion curves as a function of mode number for the fundamental modes 2–5. Only for mode 2, Fig. 7a, the curve exhibits a pronounced parabolic shape with a positive curvature near the pump, corresponding to a small but positive D_2. This indicates anomalous dispersion and is favorable for soliton formation. For mode 3, Fig. 7b, D_{int} rapidly flattens and approaches zero at higher mode numbers, corresponding to a very weakly anomalous dispersion regime, where comb formation may still occur but with reduced bandwidth due to limited phase matching. The remaining two curves display negative curvature, corresponding to $D_2 < 0$ (normal dispersion). In these cases, bright soliton formation is not possible, although other nonlinear states such as dark solitons or modulation instability may arise. The increasingly negative slope at higher mode numbers further restricts the accessible comb bandwidth for these modes.

Frequency comb generation study

We investigate the frequency comb generation both experimentally and numerically, utilizing a high-Q microresonator based on a silicon nitride (Si_3N_4) ring, again surrounded with SiO_2. The experimental setup used to obtain these measurements is described in detail in the Methods section below. The central radius of the ring resonator is $R_c = 225\,\mu m$, with a ring width of $w_r = 1.55\,\mu m$ and a height of $h_r = 0.8\,\mu m$. The straight bus waveguide, which couples light into the resonator, is not tapered and runs parallel to the tangential direction of the circular ring resonator, as illustrated in Fig. 1. The bus waveguide has identical cross-sectional dimensions ($1.55\,\mu m \times 0.8\,\mu m$). The gap between the waveguide and ring is $g = 0.5\,\mu m$. The excitation wavelength is 1.55 μm.

We first generate numerical results using a high-resolution mesh with 100 points per wavelength (ppw) sampling density. For $\lambda = 1550$ nm, the computed effective index is 1.8436. Given that the ring radius is significantly larger than the wavelength, the effective index of the first resonant mode is calculated to be 1.8448, which is very close to the effective index of the waveguide. The corresponding group index is found to be 2.1292, leading to an estimated free spectral range (FSR) of approximately 99.6 GHz, using the relation $\text{FSR}_{\text{approx}} \approx c_0/2\pi n_g R_c$.

Next, we compute the effective index across the wavelength range $1500\ \text{nm} \leq \lambda \leq 1560\ \text{nm}$ using three different discretizations: 20 ppw, 40 ppw, and 100 ppw. From these values, the integrated dispersion (D_{int}) is calculated. In Fig. 8, we present these numerical results (solid blue, dashed red, and dash-dotted yellow curves, respectively) alongside experimentally measured values (purple circles). As expected, the simulation with 100 ppw shows excellent agreement with experimental data throughout the spectrum. Reduced mesh quality leads to increasing discrepancies, particularly at wavelengths further from the pump wavelength, underscoring the importance of sufficient numerical resolution for accurate modeling.

Figure 9a shows the transmission spectrum obtained with the numerical solution of the power transmission formula[26] assuming a propagation loss of $\alpha = 0.06$ dB/cm[37] to account for material absorption, scattering, and radiation losses. The spectral difference between the two dips, in other words, the FSR, is determined to be 99.6 GHz, which agrees with the approximate number aforementioned before.

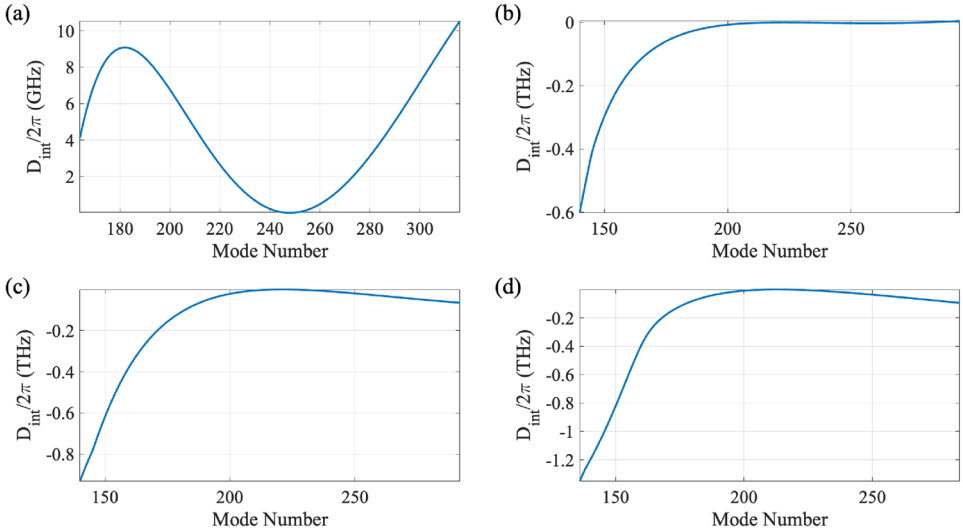

Fig. 7. (**a**)–(**d**) Integrated dispersion curves for the fundamental modes 2–5.

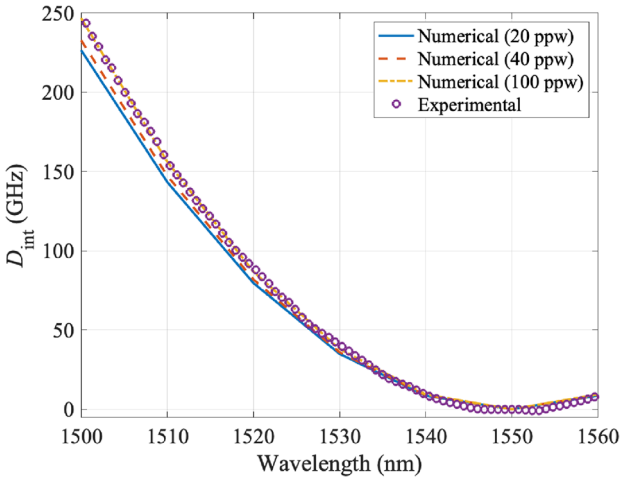

Fig. 8. Integrated dispersion (D_{int}) of a Si_3N_4 ring resonator ($R_c = 225\,\mu$m, $w_r = 1.55\,\mu$m, and $h_r = 0.8\,\mu$m) embedded in SiO_2. Numerical solutions obtained using three different mesh densities are compared against experimental results.

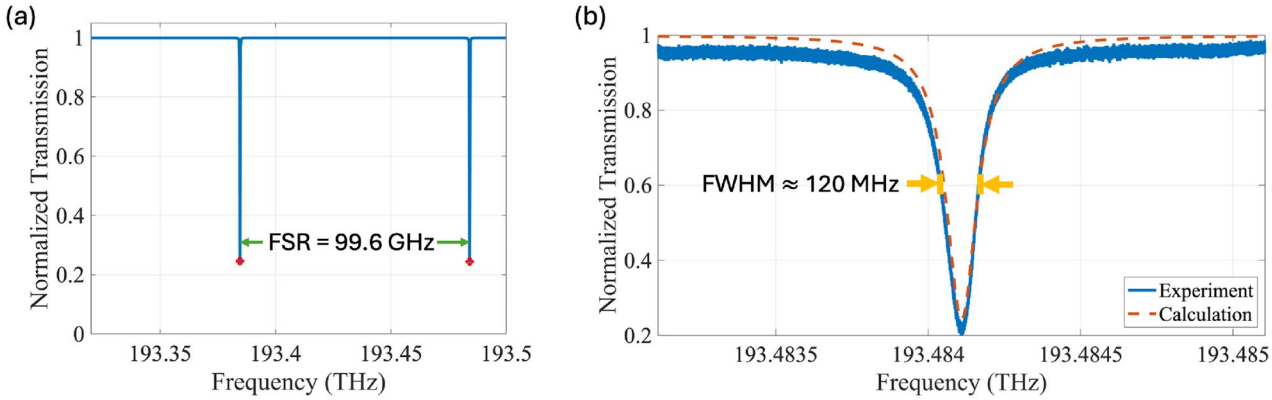

Fig. 9. (**a**) Normalized transmission vs. excitation frequency obtained with the numerical solution. (**b**) A comparison of experimental (blue) and calculated (red) transmission spectra near the resonance.

Figure 9b presents a detailed view of the resonance observed in both our numerical simulations and experimental measurements. To validate these simulations experimentally, we employed a setup with a primary pump laser operating with low power at 1550.183 nm to characterize the resonator's linewidth. However, to facilitate a direct comparison between numerical and experimental results, we aligned the frequency axis such that the strongest dip in the numerical transmission spectrum, located at 1549.5 nm, coincides with the center of the experimental data. Both results exhibit a Lorentzian shape with a linewidth (full width at half maximum) of 120 MHz. This narrow linewidth corresponds to a high quality factor (Q-factor = pump frequency/Δ_{FWHM}) of 1.6 million, indicating a highly confined resonance. It is important to note that this Q-factor represents the total or loaded quality factor, defined as $1/Q = 1/Q_{\text{c}} + 1/Q_{\text{i}}$, and is distinct from the coupling quality factor (Q_{c}) and the intrinsic resonance quality (Q_{i}) of the ring. The average coupling quality factor, which characterizes the energy transfer efficiency between the waveguide and the ring, was numerically determined to be 2.2 million.

Figure 10 presents a comparative analysis of the calculated (red sticks) and experimentally measured (blue curve) power spectra, showcasing the generation of an optical frequency comb using a bus waveguide coupled to a ring resonator.

In experiment, the primary pump laser operates at approximately 1550 nm and is tuned across the cavity resonance from the blue-detuned side to the red-detuned side to access the soliton or frequency-comb state. As the pump approaches the center of the resonance, coupling efficiency increases, leading to higher intracavity power and a transition to a chaotic regime. This elevated intracavity power induces thermal effects that shift the cavity resonance. Upon the formation of a soliton state, the intracavity energy undergoes an abrupt reduction, resulting in a rapid cooling of the resonator. Consequently, the cavity resonances "snap back" toward their original positions. Since the relative detuning between the pump and the nearest resonance is altered from the detuning value at which the soliton was first initiated, the soliton state often becomes unstable and is lost. To mitigate this instability, an auxiliary laser was introduced[38]. The auxiliary laser is positioned with a blue

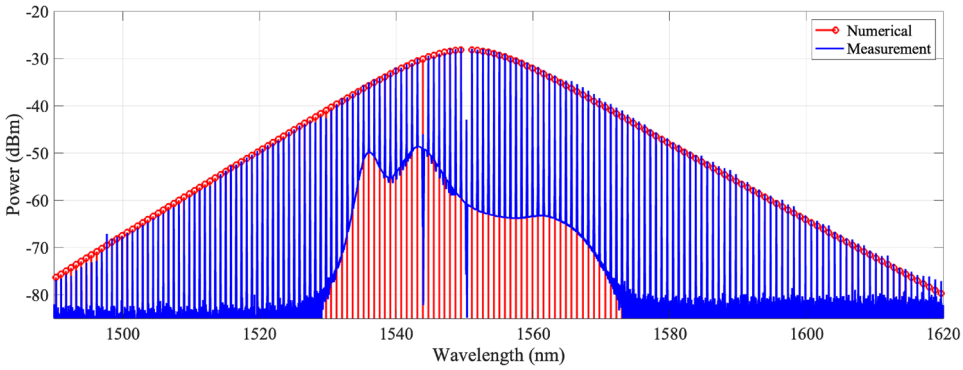

Fig. 10. Measured (blue curve) and calculated (red sticks) power density as a function wavelength.

detuning relative to a nearby resonance, in this case at 1543.71 nm, thereby providing controlled cavity heating. As the primary pump is scanned from the blue-detuned to the red-detuned side of its resonance, the resulting heating also red-shifts the resonance near the auxiliary laser wavelength. This shift decreases the coupling efficiency of the auxiliary laser into the cavity, thereby reducing its heating contribution. The net effect is a stabilization of the cavity temperature, which suppresses thermo-optic drift of the resonances, including the primary pump resonance, and enhances the stability of the soliton state. The experimental result shown in Fig. 10 was obtained by pumping the bus waveguide with 300 mW at 1550.183 nm while simultaneously applying an auxiliary laser at 1543.71 nm with 263 mW. For the LLE solution, we assume $\delta_0 = 3.2$, $F = 2.2$, $D_2 = -0.01$, and $\gamma = 0.8$ (for details, please see "Supplementary Information"). Both the simulation and experimental data confirm the formation of a frequency comb with an FSR of 99.6 GHz, demonstrating excellent agreement in this fundamental characteristic.

The calculated spectrum (red sticks) displays a highly regular and idealized comb structure characterized by sharp spectral lines with a hyperbolic-secant shape spanning a wide bandwidth. This spectrum represents the intrinsic behavior of the system as predicted by the LLE under ideal conditions. In contrast, the experimentally obtained spectrum (blue curve) exhibits deviations from this ideal scenario. Notably, the noise floor is significantly higher in the experimental data, reflecting noise sources not captured in the simulations. While part of this elevation may be linked to reduced signal levels at the detectors due to coupling and insertion losses, it may also arise from amplified spontaneous emission noise introduced by the EDFAs used to boost both the pump and auxiliary lasers. This differs from the simulations, where the entire signal output is plotted after filtering out the pump and no amplifier noise is present. The experimental spectrum exhibits additional spectral features, including dips and broadened peaks, that are not present in the calculated results. These deviations may arise from various factors, including fabrication imperfections[39], thermal fluctuations[2], photodetector noise[40,41], and non-ideal coupling conditions[42]. For instance, variations in the waveguide dimensions or surface roughness can lead to scattering losses and resonance shifts, affecting the comb's spectral profile[39]. Similarly, temperature fluctuations can induce changes in the refractive index, altering the cavity's resonance frequencies[2]. It is important to note that both the primary pump and auxiliary laser peaks are filtered out in the experimental spectrum using fiber Bragg grating filters. The observed spectral features, along with the power-related noise floor, provide valuable insights into the non-ideal behavior of the fabricated device and highlight the challenges associated with achieving perfect agreement between simulations and experiments.

Methods

Numerical model

The electric (E) and magnetic (H) field components of the electromagnetic wave propagating inside the dielectric ring can be represented as sums of three orthogonal vectors as follows

$$\mathrm{E}(\rho,\phi,z) = \left\{\hat{\rho}E_\rho(\rho,z) + \hat{\phi}E_\phi(\rho,z) + \hat{z}E_z(\rho,z)\right\} e^{-j\nu\phi}, \tag{1}$$

$$\mathrm{H}(\rho,\phi,z) = \left\{\hat{\rho}H_\rho(\rho,z) + \hat{\phi}H_\phi(\rho,z) + \hat{z}H_z(\rho,z)\right\} e^{-j\nu\phi}, \tag{2}$$

assuming $e^{-j\nu\phi}$ dependence, ν is the angular propagation constant, ρ is the radial distance from the origin to the point projected onto the xy plane, ϕ is the azimuthal angle, and z is the height or vertical distance from the xy plane. Our goal is to determine the ν and to compute the propagating modes (E and H) along the ϕ direction inside the dielectric ring for a given frequency (f), corresponding to the wavelength $\lambda = c_0/f$, where c_0 is the velocity of electromagnetic waves in vacuum.

To carry out modal analysis, we start with Maxwell's equations to derive the Helmholtz wave equations for the electric and magnetic fields in a source-free, lossless, and non-magnetic medium. After expanding each term of the electric field equation, we obtain the following three sets of scalar equations by enforcing each side of the equation to be the same in the $\hat{\rho}$, $\hat{\phi}$, and $\hat{z}$ directions:

$\hat{\rho}$ direction:

$$\left(\mathcal{L}-\frac{1}{R_c^2}+\frac{\rho^2}{R_c^2}\frac{\partial}{\partial\rho}\frac{1}{\varepsilon}\frac{\partial\varepsilon}{\partial\rho}\right)E_\rho+\frac{2j\beta}{R_c}E_\phi+\frac{\rho^2}{R_c^2}\frac{\partial}{\partial\rho}\frac{1}{\varepsilon}\frac{\partial\varepsilon}{\partial z}E_z=\beta^2E_\rho, \tag{3}$$

$\hat{\phi}$ direction:

$$\left(-\frac{2j\beta}{R_c}-\frac{j\beta\rho}{R_c\varepsilon}\frac{\partial\varepsilon}{\partial\rho}\right)E_\rho+\left(\mathcal{L}-\frac{1}{R_c^2}\right)E_\phi-\frac{j\beta\rho}{R_c\varepsilon}\frac{\partial\varepsilon}{\partial z}E_z=\beta^2E_\phi, \tag{4}$$

$\hat{z}$ direction:

$$\frac{\rho^2}{R_c^2}\frac{\partial}{\partial z}\frac{1}{\varepsilon}\frac{\partial\varepsilon}{\partial\rho}E_\rho+\mathcal{L}E_z+\frac{\rho^2}{R_c^2}\frac{\partial}{\partial z}\frac{1}{\varepsilon}\frac{\partial\varepsilon}{\partial z}E_z=\beta^2E_z, \tag{5}$$

where

$$\mathcal{L}=\frac{\rho^2}{R_c^2}\left(\frac{\partial^2}{\partial\rho^2}+\frac{1}{\rho}\frac{\partial}{\partial\rho}+\frac{\partial^2}{\partial z^2}+k_0^2\varepsilon_r\right). \tag{6}$$

Following a similar procedure on the Helmholtz wave equation for the magnetic field, we obtain three other equations. However, since we will only need the one along the $\hat{z}$ direction, we provide it below for the sake of completeness.

$$\frac{\rho^2}{R_c^2}\frac{1}{\varepsilon}\frac{\partial\varepsilon}{\partial\rho}\frac{\partial H_\rho}{\partial z}+\left(\mathcal{L}-\frac{\rho^2}{R_c^2}\frac{1}{\varepsilon}\frac{\partial\varepsilon}{\partial\rho}\frac{\partial}{\partial\rho}\right)H_z=\beta^2H_z. \tag{7}$$

It is known that mixed electric field–magnetic field formulations allow for direct enforcement of boundary conditions on both electric and magnetic fields at interfaces between materials[16]. In single-field formulations, deriving the secondary field (electric from magnetic or vice versa) often complicates boundary condition enforcement, introducing errors at material interfaces[25]. From Maxwell's equations, one can derive the following expressions:

$$E_\phi=\frac{1}{j\omega\varepsilon}\left(\frac{\partial H_\rho}{\partial z}-\frac{\partial H_z}{\partial\rho}\right), \tag{8}$$

$$H_\phi=\frac{1}{j\omega\mu_0}\left(\frac{\partial E_z}{\partial\rho}-\frac{\partial E_\rho}{\partial z}\right). \tag{9}$$

By using Eq. (8), we rewrite Eq. (3) in the following form

$$\left(\mathcal{L}-\frac{1}{R_c^2}+\frac{\rho^2}{R_c^2}\frac{\partial}{\partial\rho}\frac{1}{\varepsilon}\frac{\partial\varepsilon}{\partial\rho}\right)E_\rho+\left(\frac{\rho^2}{R_c^2}\frac{\partial}{\partial\rho}\frac{1}{\varepsilon}\frac{\partial\varepsilon}{\partial z}\right)E_z+\frac{2\beta}{\omega\varepsilon R_c}\left(\frac{\partial H_\rho}{\partial z}-\frac{\partial H_z}{\partial\rho}\right)=\beta^2E_\rho. \tag{10}$$

Similarly, $\hat{\rho}$ component of the H-formulation becomes

$$\left(\mathcal{L}-\frac{\rho^2}{R_c^2}\frac{1}{\varepsilon}\frac{\partial\varepsilon}{\partial z}\frac{\partial}{\partial z}-\frac{1}{R_c^2}\right)H_\rho+\frac{\rho^2}{R_c^2}\frac{1}{\varepsilon}\frac{\partial\varepsilon}{\partial z}\frac{\partial}{\partial z}H_z+\frac{2\beta}{\omega\mu_0R_c}\left(\frac{\partial E_z}{\partial\rho}-\frac{\partial E_\rho}{\partial z}\right)=\beta^2H_\rho. \tag{11}$$

Equations (10), (11), (5), and (7) can be cast into a matrix equation such as

$$\overline{\overline{M}}\mathrm{A}+\beta\overline{\overline{L}}\mathrm{A}-\beta^2\overline{\overline{I}}\mathrm{A}=0, \tag{12}$$

where $\mathrm{A}=[E_\rho\ E_z\ H_\rho\ H_z]^T$, $\overline{\overline{M}}$ is the matrix independent of β, $\overline{\overline{L}}$ is the linear term in β, and the last term is the quadratic term in β.

$$\overline{\overline{M}}=\begin{bmatrix}M_1 & M_2 & 0 & 0\\ M_3 & M_4 & 0 & 0\\ 0 & 0 & M_5 & M_6\\ 0 & 0 & M_7 & M_7\end{bmatrix} \tag{13}$$

$$\overline{\overline{L}}=\begin{bmatrix}0 & 0 & L_1 & L_2\\ 0 & 0 & 0 & 0\\ L_3 & L_4 & 0 & 0\\ 0 & 0 & 0 & 0\end{bmatrix} \tag{14}$$

$$M_1=\mathcal{L}-\frac{1}{R_c^2}+\frac{\rho^2}{R_c^2}\frac{\partial}{\partial\rho}\frac{1}{\varepsilon}\frac{\partial\varepsilon}{\partial\rho} \tag{15}$$

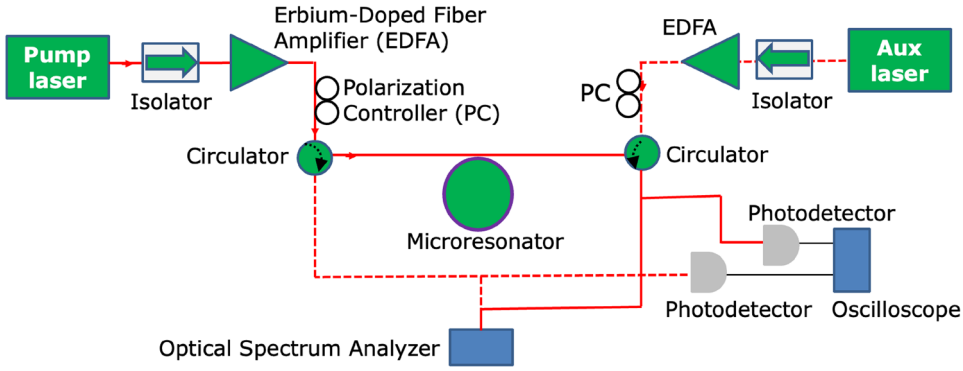

Fig. 11. Schematic of the experimental setup for frequency comb generation and analysis. The red solid lines indicate the primary laser path for soliton frequency comb generation, while the red dashed lines represent the auxiliary laser used to compensate for the resonator's thermal shift. The output is analyzed using photodetectors, an oscilloscope, and an optical spectrum analyzer.

$$M_2 = \frac{\rho^2}{R_c^2}\frac{\partial}{\partial\rho}\frac{1}{\varepsilon}\frac{\partial\varepsilon}{\partial z} \tag{16}$$

$$M_3 = \frac{\rho^2}{R_c^2}\frac{\partial}{\partial z}\frac{1}{\varepsilon}\frac{\partial\varepsilon}{\partial\rho} \tag{17}$$

$$M_4 = \mathcal{L} + \frac{\rho^2}{R_c^2}\frac{\partial}{\partial z}\frac{1}{\varepsilon}\frac{\partial\varepsilon}{\partial z} \tag{18}$$

$$M_5 = \mathcal{L} - \frac{\rho^2}{R_c^2}\frac{1}{\varepsilon}\frac{\partial\varepsilon}{\partial z}\frac{\partial}{\partial z} - \frac{1}{R_c^2} \tag{19}$$

$$M_6 = \frac{\rho^2}{R_c^2}\frac{1}{\varepsilon}\frac{\partial\varepsilon}{\partial z}\frac{\partial}{\partial z} \tag{20}$$

$$M_7 = \frac{\rho^2}{R_c^2}\frac{1}{\varepsilon}\frac{\partial\varepsilon}{\partial\rho}\frac{\partial}{\partial z} \tag{21}$$

$$M_8 = \mathcal{L} - \frac{\rho^2}{R_c^2}\frac{1}{\varepsilon}\frac{\partial\varepsilon}{\partial\rho}\frac{\partial}{\partial\rho} \tag{22}$$

$$L_1 = \frac{2\beta}{\omega\varepsilon R_c}\frac{\partial H_\rho}{\partial z} \tag{23}$$

$$L_2 = -\frac{2\beta}{\omega\varepsilon R_c}\frac{\partial H_z}{\partial\rho} \tag{24}$$

$$L_3 = -\frac{2\beta}{\omega\mu_0 R_c}\frac{\partial}{\partial z} \tag{25}$$

$$L_4 = \frac{2\beta}{\omega\mu_0 R_c}\frac{\partial}{\partial\rho} \tag{26}$$

This can be rewritten as a linear generalized eigenvalue problem by introducing an auxiliary variable $\mathrm{F} = \beta\mathrm{A}$, leading to $\overline{\overline{M}}\mathrm{A} + \overline{\overline{L}}\mathrm{F} - \mathrm{F}\beta = 0$, which gives the augmented system:

$$\begin{pmatrix} \overline{\overline{M}} & \overline{\overline{L}} \\ 0 & \overline{\overline{I}} \end{pmatrix} \begin{pmatrix} \mathrm{A} \\ \mathrm{F} \end{pmatrix} = \beta \begin{pmatrix} 0 & \overline{\overline{I}} \\ \overline{\overline{I}} & 0 \end{pmatrix} \begin{pmatrix} \mathrm{A} \\ \mathrm{F} \end{pmatrix}. \tag{27}$$

We solve this linear generalized eigenvalue problem using MATLAB's eigs function, which is optimized for large sparse matrices. After solving, we retain only the physically meaningful modes (those with $n_{\mathrm{eff}}^{\mathrm{ring}} < n_{\mathrm{ring}}$, where $n_{\mathrm{eff}}^{\mathrm{ring}} = \beta/k_0$ is the effective index of the ring and n_{ring} is the refractive index of the material which ring is made from.)

Experiment setup

Figure 11 illustrates the experimental configuration used to study the dynamics of frequency comb generation in a dielectric waveguide coupled to a dielectric ring resonator. A primary pump laser initiates the generation

of soliton frequency combs by leveraging nonlinear effects like Kerr nonlinearity and four-wave mixing within this system. To enhance stability and widen the operational range for solitons, an auxiliary laser is employed to regulate resonator power[38]. Each laser source is protected from back reflections by optical isolators positioned at its output. The pump light's intensity is increased by an erbium-doped fiber amplifier (EDFA) before being coupled into the microresonator using a circulator. A second circulator performs two roles: it directs the output light to various measurement devices and allows the auxiliary laser to enter the resonator propagating counter to the primary pump. The optical output is converted to electrical signals by two photodetectors, enabling time-domain analysis of the pulse train with an oscilloscope. Simultaneously, an optical spectrum analyzer measures the spectral features of the generated frequency comb. Before optical measurement, the strong residual pump and auxiliary peaks are removed from the optical spectrum using fiber Bragg grating filters (AOS), which provide a tuning range of approximately 10 nm (center wavelength ±5 nm), a FWHM bandwidth of ∼30–35 GHz, and a rejection ratio exceeding 38 dB.

Discussions

Our numerical method is highly accurate for simple geometries such as rectangles and circles in the ρ-z plane, where a 40 ppw grid is sufficient. Complex shapes require higher densities; we recommend starting at 40 PPW and increasing by 10 PPW until eigenvalues converge. For non-rectangular cross-sections (e.g., trapezoids in the $\rho - z$ plane), a rectangular mesh causes geometric inaccuracies ("stair-step" effect), impacting boundary precision, the effective refractive index, and is especially problematic for higher-order azimuthal modes, potentially causing spurious effects.

When comparing these two methods, FEM vs. FDFD, we can confidently state that the more accurate and reliable approach for modal analysis is the FEM, which is renowned for its ability to handle complex geometries, material interfaces, and boundary conditions with high precision. Its flexibility in mesh adaptation and the use of higher-order interpolation functions makes it particularly suitable for problems requiring high accuracy, especially in regions with sharp field variations or subwavelength features. However, for large-scale parametric studies–such as simulating hundreds of ring resonator designs across tens of wavelength values–the FDFD method offers a compelling trade-off between accuracy and computational efficiency. When implemented on high-quality, sufficiently refined grids, FDFD can produce results comparable to FEM in terms of accuracy. Moreover, due to its use of regular grids and simpler basis functions (typically piecewise constant or linear), FDFD solvers are often faster and require less memory than FEM solvers. This makes FDFD particularly advantageous for inverse design, optimization loops, or rapid prototyping scenarios that require thousands of simulations.

Conclusion

In this work, we presented a novel finite-difference frequency-domain formulation for electromagnetic modal analysis in dielectric ring resonators, addressing key limitations of existing methods. Our approach solves for both electric and magnetic fields simultaneously in cylindrical coordinates, eliminating spurious modes and ensuring accurate field solutions–particularly at material boundaries where earlier formulations failed. By avoiding coordinate transformations and retaining all field components, our method provides a complete description of hybrid modes, crucial for modeling microresonators used in optical frequency comb generation. We validated our solver through rigorous benchmarks against COMSOL Multiphysics, Tidy3D, and experimental data, demonstrating excellent agreement in effective refractive indices, dispersion profiles, and resonance characteristics. Notably, our method automates mode computation without requiring manual input for azimuthal mode numbers, significantly streamlining the design process. Applied to Si_3N_4 ring resonators, our solver accurately predicted anomalous dispersion near 1060 nm and reproduced experimental free spectral ranges and linewidths at 1550 nm, confirming its utility for Kerr frequency comb design.

Data availability

The code to reproduce the results provided in this manuscript can be found at https://github.com/simsekergun/DieRingSolver

Received: 13 June 2025; Accepted: 4 September 2025
Published online: 08 October 2025

References

1. Holzwarth, R. et al. Optical frequency synthesizer for precision spectroscopy. *Phys. Rev. Lett.* **85**, 2264–2267. https://doi.org/10.1103/PhysRevLett.85.2264 (2000).
2. Kippenberg, T. J., Holzwarth, R. & Diddams, S. A. Microresonator-based optical frequency combs. *Science* **332**, 555–559. https://doi.org/10.1126/science.1193968 (2011).
3. Picqué, N. & Hänsch, T. W. Frequency comb spectroscopy. *Nat. Photonics* **13**, 146–157. https://doi.org/10.1038/s41566-018-0347-5 (2019).
4. Luke, K., Okawachi, Y., Lamont, M. R. E., Gaeta, A. L. & Lipson, M. Broadband mid-infrared frequency comb generation in a Si_3N_4 microresonator. *Opt. Lett.* **40**, 4823–4826. https://doi.org/10.1364/OL.40.004823 (2015).
5. Udem, T., Holzwarth, R. & Hänsch, T. W. Optical frequency metrology. *Nature* **416**, 233–237. https://doi.org/10.1038/416233a (2002).
6. Moille, G. et al. Versatile optical frequency division with kerr-induced synchronization at tunable microcomb synthetic dispersive waves. *Nat. Photonics* **19**, 36–43. https://doi.org/10.1038/s41566-024-01540-w (2025).
7. Kues, M. et al. Quantum optical microcombs. *Nat. Photonics* **13**, 170–179. https://doi.org/10.1038/s41566-019-0363-0 (2019).
8. Herr, T. et al. Universal formation dynamics and noise of Kerr-frequency combs in microresonators. *Nat. Photonics* **6**, 480–487. https://doi.org/10.1038/nphoton.2012.127 (2012).

9. Moille, G. et al. Broadband resonator-waveguide coupling for efficient extraction of octave-spanning microcombs. *Opt. Lett.* **44**, 4737–4740. https://doi.org/10.1364/OL.44.004737 (2019).
10. Chembo, Y. K. Kerr optical frequency combs: Theory, applications and perspectives. *Nanophotonics* **5**, 214–230 (2016).
11. Taflove, A. & Hagness, S. C. *Computational Electrodynamics: The Finite-Difference Time-Domain Method* (Artech House, 2005).
12. Rahman, B. M. A., Leung, D. M. H., Obayya, S. S. A. & Grattan, K. T. V. Numerical analysis of bent waveguides: bending loss, transmission loss, mode coupling, and polarization coupling. *Appl. Opt.* **47**, 2961–2970. https://doi.org/10.1364/AO.47.002961 (2008).
13. Jin, J.-M. *The finite element method in electromagnetics*, chap. 7 (Wiley-IEEE, 2002).
14. Kakihara, K., Kono, N., Saitoh, K. & Koshiba, M. Full-vectorial finite element method in a cylindrical coordinate system for loss analysis of photonic wire bends. *Opt. Express* **14**, 11128–11141. https://doi.org/10.1364/OE.14.011128 (2006).
15. Simsek, E., Liu, J. & Liu, Q. A spectral integral method and hybrid SIM/FEM for layered media. *IEEE Trans. Microw. Theory Tech.* **54**, 3878–3884. https://doi.org/10.1109/TMTT.2006.883647 (2006).
16. Notaros, B. M. Higher order frequency-domain computational electromagnetics. *IEEE Trans. Antennas Propag.* **56**, 2251–2276. https://doi.org/10.1109/TAP.2008.926784 (2008).
17. Prkna, L., Hubalek, M. & Ctyroky, J. Vectorial eigenmode solver for bent waveguides based on mode matching. *IEEE Photonics Technol. Lett.* **16**, 2057–2059. https://doi.org/10.1109/LPT.2004.831565 (2004).
18. Pascher, W. & Pregla, R. Vectorial analysis of bends in optical strip waveguides by the method of lines. *Radio Sci.* **28**, 1229–1233. https://doi.org/10.1029/93RS01829 (1993).
19. Kim, S. & Gopinath, A. Vector analysis of optical dielectric waveguide bends using finite-difference method. *J. Lightwave Technol.* **14**, 2085–2092. https://doi.org/10.1109/50.536977 (1996).
20. Xiao, J., Ni, H. & Sun, X. Full-vector mode solver for bending waveguides based on the finite-difference frequency-domain method in cylindrical coordinate systems. *Opt. Lett.* **33**, 1848–1850. https://doi.org/10.1364/OL.33.001848 (2008).
21. Xiao, J., Ma, H., Bai, N., Liu, X. & Sun, X. Full-vectorial analysis of bending waveguides using finite difference method based on H-fields in cylindrical coordinate systems. *Opt. Commun.* **282**, 2511–2515. https://doi.org/10.1016/j.optcom.2009.03.040 (2009).
22. Xiao, J. & Sun, X. Full-vector analysis of optical dielectric waveguide bends using improved finite difference method based on E fields in cylindrical coordinate systems. *J. Opt.* **12**, 055404. https://doi.org/10.1088/2040-8978/12/5/055404 (2010).
23. Xiao, J. & Sun, X. Vector analysis of bending waveguides by using a modified finite-difference method in a local cylindrical coordinate system. *Opt. Express* **20**, 21583–21597. https://doi.org/10.1364/OE.20.021583 (2012).
24. Wu, X. & Xiao, J. Full-vector analysis of bending waveguides by using meshless finite cloud method in a local cylindrical coordinate system. *J. Lightwave Technol.* **39**, 7199–7209. https://doi.org/10.1109/JLT.2021.3109889 (2021).
25. Simsek, E. Practical vectorial mode solver for dielectric waveguides based on finite differences. *Opt. Lett.* **50**, 4102–4105. https://doi.org/10.1364/OL.550820 (2025).
26. Yariv, A. Critical coupling and its control in optical waveguide-ring resonator systems. *IEEE Photonics Technol. Lett.* **14**, 483–485. https://doi.org/10.1109/68.992585 (2002).
27. Hammer, M., Hiremath, K. R. & Stoffer, R. Analytical approaches to the description of optical microresonator devices. *AIP Conf. Proc.* **709**, 48–71. https://doi.org/10.1063/1.1764013 (2004).
28. Lugiato, L. A. & Lefever, R. Spatial dissipative structures in passive optical systems. *Phys. Rev. Lett.* **58**, 2209 (1987).
29. Chembo, Y. K. & Yu, N. Modal expansion approach to optical-frequency-comb generation with monolithic whispering-gallery-mode resonators. *Phys. Rev. A* **82**, 033801. https://doi.org/10.1103/PhysRevA.82.033801 (2010).
30. Chembo, Y. K. & Menyuk, C. R. Spatiotemporal Lugiato-Lefever formalism for Kerr-comb generation in whispering-gallery-mode resonators. *Phys. Rev. A* **87**, 053852 (2013).
31. Castelli, F., Brambilla, M., Gatti, A., Prati, F. & Lugiato, L. A. The lle, pattern formation and a novel coherent source. *Eur. Phys. J. D* **71**, 84. https://doi.org/10.1140/epjd/e2017-70754-1 (2017).
32. Cole, D. C., Gatti, A., Papp, S. B., Prati, F. & Lugiato, L. Theory of kerr frequency combs in fabry-perot resonators. *Phys. Rev. A* **98**, 013831. https://doi.org/10.1103/PhysRevA.98.013831 (2018).
33. Lui, W., Xu, C.-L., Hirono, T., Yokoyama, K. & Huang, W.-P. Full-vectorial wave propagation in semiconductor optical bending waveguides and equivalent straight waveguide approximations. *J. Lightw. Technol.* **16**, 910–914 (1998).
34. Berenger, J.-P. A perfectly matched layer for the absorption of electromagnetic waves. *J. Comput. Phys.* **114**, 185–200. https://doi.org/10.1006/jcph.1994.1159 (1994).
35. Kogelnik, H. Theory of dielectric waveguides. In *Integrated Optics* 13–81 (Springer, 1975).
36. Malitson, I. H. Interspecimen comparison of the refractive index of fused silica⁎,†. *J. Opt. Soc. Am.* **55**, 1205–1209. https://doi.org/10.1364/JOSA.55.001205 (1965).
37. Krückel, C. J. et al. Continuous wave-pumped wavelength conversion in low-loss silicon nitride waveguides. *Opt. Lett.* **40**, 875–878. https://doi.org/10.1364/OL.40.000875 (2015).
38. Zhang, S. et al. Sub-milliwatt-level microresonator solitons with extended access range using an auxiliary laser. *Optica* **6**, 206–212. https://doi.org/10.1364/OPTICA.6.000206 (2019).
39. Moille, G., Westly, D., Orji, N. G. & Srinivasan, K. Tailoring broadband kerr soliton microcombs via post-fabrication tuning of the geometric dispersion. *Appl. Phys. Lett.* **119**, 526 (2021).
40. Simsek, E. et al. Fast evaluation of RF power spectrum of photodetectors with windowing functions. *IEEE Trans. Electron. Dev.* **70**, 3643–3648. https://doi.org/10.1109/TED.2023.3275553 (2023).
41. Anjum, I. M. et al. Use of evolutionary optimization algorithms for the design and analysis of low bias, low phase noise photodetectors. *J. Lightwave Technol.* **41**, 7285–7291. https://doi.org/10.1109/JLT.2023.3330099 (2023).
42. Cheung, S. et al. Demonstration of a 17× 25 gb/s heterogeneous III-V/Si DWDM transmitter based on (de-) interleaved quantum dot optical frequency combs. *J. Lightwave Technol.* **40**, 6435–6443 (2022).

Acknowledgements

This work has been supported in part by cooperative agreements with the National Center for Manufacturing Sciences 2022138-142232 and 2023200-142386, which are sub-contracts from the US-DoD cooperative agreements HQ0034-20-2-0007 and HQ0034-24-2-0001, respectively. The authors acknowledge useful discussions with J. P. Cahill, T. Mahmood, and W. Zhou of the Army Research Laboratory and G. Moille and K. Srinivasan of NIST and UMD-JQI.

Author contributions

E.S. developed the formulation and implemented it in MATLAB. A.N. and G.M.C. built the experiment setup and conducted the measurements. R.I. and L.C. carried out numerical simulations. P.S. helped with the LLE calculations. E.S. and C.R.M. wrote the first draft of the manuscript. All authors worked together on the final version of the manuscript.

Competing interests
The authors declare no competing interests.

Additional information
Supplementary Information The online version contains supplementary material available at https://doi.org/10.1038/s41598-025-18869-z.

Correspondence and requests for materials should be addressed to E.S.

Reprints and permissions information is available at www.nature.com/reprints.

Publisher's note Springer Nature remains neutral with regard to jurisdictional claims in published maps and institutional affiliations.